Localized corrosion induced surface modifications of Al-Cu-Li alloy studied by ToF-SIMS 3D imaging

Meicheng Li, Antoine Seyeux, Frédéric Wiame, Philippe Marcus, Jolanta Światowska

Localized corrosion induced surface modifications of Al-Cu-Li alloy studied by ToF-SIMS 3D imaging

Meicheng Li, Antoine Seyeux, Frédéric Wiame, Philippe Marcus and Jolanta Światowska*

Chimie ParisTech - CNRS, PSL University, Institut de Recherche de Chimie Paris,

11 rue Pierre et Marie Curie, 75005 Paris, France

Abstract

Three-dimensional (3D) time-of-flight secondary ion mass spectrometry (ToF-SIMS) imaging is a promising tool in analysis of surface modifications of alloy matrix and intermetallic particles induced by localized corrosion due to its good spatial resolution and very high sensitivity to chemical identification especially involving light mass elements like Li. In this paper, ToF-SIMS 3D chemical mapping combined with scanning electron microscopy (SEM) was performed to study the localized corrosion of Al-Cu-Li alloy (AA2050-T8) in a region of Al-Cu-Fe-Mn intermetallic particle (IMP) in 0. 1M NaCl solution. Initiation of corrosion was locally observed on the IMPs and between IMPs and matrix substrate. Moreover, a modified oxide/hydroxide layer was observed over IMPs compared to the matrix. This new corrosion layer was enriched with chlorides and Cu hydroxides. ToF-SIMS 3D imaging revealed that Li was present in the alloy matrix, while no Li was present in the IMPs in regions where localized corrosion occurred.

Keywords: ToF-SIMS; three-dimensional (3D) chemical mapping; localized corrosion; Al-Cu-Li alloy; intermetallic particles.

* Corresponding author: jolanta.swiatowska@chimieparistech.psl.eu

1 Introduction

Localized corrosion of Al alloys is known to be the most frequent cause of failure of high-strength aluminium alloys [1,2]. The less common intergranular or transgranular corrosion can be also considered as a precursor of stress corrosion cracking (SCC) or a potential origin for fatigue cracks [3-6]. The corrosion is not only a lateral surface modifications and breakdown of surface oxide but also can lead to in-depth modifications of the oxide and undermining alloy. The localized corrosion is generally related to the chemical heterogeneities in the alloy such as intermetallic particles (IMPs). It has been shown that the Al-Cu-Fe-Mn IMPs are the preferential sites of localized corrosion initiation in Al alloys due to the galvanic effect [3-6]. However, it is widely known that cathodic can become negative during exposure to corrosive media [7]. Birbilis *et al.* [8] revealed that the initially cathodic Al-Cu-Fe IMPs in AA7075 leads to the localized corrosion between matrix and IMPs termed trenching. This peripheral corrosion is also often referred to as 'cathodic corrosion' [9]. In further stages intergranular corrosion attack, and/or exfoliation can develop [10]. However, here a discussion on more advanced stages of corrosion is beyond this paper. Boag *et al*. [11] have also shown that preferential corrosion sites of the AA2024 Al-Cu-Mg alloy in NaCl electrolyte are associated with the presence of Al-Cu-Fe-Mn particles. This IMP-induced localized corrosion has been usually investigated by conventional techniques such as scanning electron microscopy (SEM), energy-dispersive X-ray spectroscopy (EDX) [12,13]. Some local techniques such as atomic force microscopy (AFM) [14], scanning Auger spectroscopy [15], and scanning Kelvin probe force microscopy (SKPFM) [16,17], and especially *in situ* techniques such as *in situ* SKPFM [7] can focus more precisely on local morphological or chemical surface modifications to reveal the influence of IMPs on the corrosion behavior of Al alloys.

Based on the current state of the art, several 3D imaging techniques can be highlighted such as scanning transmission electron microscopy (STEM), X-ray computed tomography (XCT), etc. [18-21]. In electron microscopy tomography (EMT), a series of EMT images from the same sample can be collected through a wide range of angles and depth from which a 3D image can be reconstructed. The corrosion behaviour of cast aluminium alloy A356 and 316L stainless steel [22-26] was studied by means of EMT and X-ray CT, respectively, to reveal the 3D spatial structure of a corrosion sites. However, these works demonstrates morphological and structural modifications induced by corrosion and pretreatment such as de-alloying of S phase (Al_2CuMg) particles in an

AA 2024-T3 aluminium alloy with preferential dissolution of Mg and Al leading to formation of a sponge-like structure with a nanosize porosity with Cu enrichment [22]. More advanced analysis methods but also focused on the microstructure can be synchrotron X-ray tomography, which is a well-established and non-destructive technique with the relatively high resolution in the range of micrometer [27,28].

ToF-SIMS three-dimensional (3D) imaging, applied here in this study, is the surface sensitive technique allowing for analysis of the low amount (in the range of ppm or even ppb) of light mass elements. It can be applied for analysis of all types of solids. It is a unique method allowing to obtain explicit information on the surface and in-depth chemical structure and elemental distribution in order to better understand the corrosion mechanisms of heterogeneous materials. A dual-beam mode allows for the spatial detection and in-depth distributions of elements in 3D space [29]. This technique has been used in various applications, such as biological, medical and chemical [30-35]. Concerning the corrosion behaviour and surface treatments, 3D ToF-SIMS imaging was used to study the localized corrosion behaviour of Mg (99%) [36] and Mg alloy [37], respectively, and showed the influence of very low amount of metallic impurities non-homogenously distributed (Fe, Mn, Al) at the grain boundaries (GBs) on different corrosion activity of GBs.

Different chemical structures of the passive film [38] or trivalent conversion coating over IMP and Al matrix of AA2024 are revealed by ToF-SIMS 3D imaging [39]. The local surface heterogeneities such as various IMPs in Al alloy matrix [40, 41] have a paramount importance in the formation of oxide layer with different composition and can lead to different surface reactivity and the localized corrosion. The objective is to understand the specific mechanisms that take place in surface heterogeneities, which are responsible for local surface breakdown. Thus, ToF-SIMS is an appropriate surface sensitive technique, which can be applied to perform a systematic set of measurement on different types of heterogeneities. Moreover, due to the high detection limits of light elements, this technique is also widely applied for analysis of Li in the Li-containing alloys [42,43] or Li in electrode materials used in Li-ion batteries [44,45]. Therefore, based on the high sensitivity to low-atomic-mass element like Li and the applicability of spatial detection, ToF-SIMS chemical imaging is considered as a promising technique for the study of Al-Cu-Li alloys.

In this paper, ToF-SIMS 3D imaging was combined with SEM/EDX characterization to study the surface modifications of AA2050-T8 (Al-Cu-Li) alloy during the first stages of corrosion. The goal of this paper is to show the application of the surface sensitive technique with a relative good lateral resolution in localized corrosion studies of heterogeneous materials in order to obtain new

information and/or to confirm some existing hypothesis in mechanistic discussion. The local surface and in-depth chemical modifications are discussed including low-atomic-mass species. To do so the same sample are termed 'a region of interest (ROI)' including an Al-Cu-Fe-Mn intermetallic particle (IMP) and surrounding matrix was selected and characterized before and after immersion in 0.1M NaCl.

2 Experimental

Samples

AA2050-T8 (Al-Cu-Li) alloy plate (with thickness of 3 mm) provided by Constellium, France was cut to specimens of 8.0 mm × 8.5 mm. The specification of alloy is presented in table 1. The samples were ground with SiC papers down to 4000-grit size (EU grades), followed by polishing using alumina suspensions down to 0.3 μm particle size to achieve mirror-surface finishing. Then, the samples were successively sonicated in iso-propanol, ethanol and finally Ultrapure (UP) Millipore water, and then dried by a stream of filtered compressed air. Then, the samples were immersed at room temperature (~25 °C) in 0.1 M NaCl electrolyte of around 75 ml (VWR, 99.9% & UP Millipore® water, resistivity > 18 MΩ cm) for 45 minutes. Then, the specimens were taken out from the solution and rinsed with UP Millipore® water, dried and transferred for ToF-SIMS and/or SEM analysis.

Table 1: Specifications (wt%) of Alloying elements in AA2050 alloys.

Element	Cu	Li	Mg	Zn	Mn	Ag	Zr(max)	Fe(max)	Si (max)
wt%	3.2–3.9	0.7–1.3	0.2–0.6	0–0.25	0.2–0.5	0.2–0.7	0.14	0.1	0.08

Surface characterization

ToF-SIMS measurements were performed with an IONTOF ToFSIMS[5] spectrometer (IONTOF GmbH, Münster, Germany) operated under high vacuum (10^{-9} mbar). A region of interest (ROI) with Al-Cu-Fe-Mn IMP was first identified. A fiducial marker was labelled on the surface using the Cs^+ ions of the Ion-ToF spectrometer for cross-correlative image tracking. The Al-Cu-Fe-Mn

IMP nearby the marker was first (before immersion test) characterized by SEM and EDX, then the sample was transferred to the ToF-SIMS analysis chamber and the same IMP with surrounding matrix was analyzed by 2D ToF-SIMS chemical imagining (without surface degradation). After immersion test in NaCl electrolyte, 3D ToF-SIMS imaging was performed. To do so, a dual beam mode with pulsed Bi^+ and Cs^+ beams (primary ion beam and sputtering beam, respectively) under burst alignment image mode was used to acquire chemical mapping, allowing a good spatial resolution of ~200 nm at moderate primary currents. For a good mass resolution, the initially wide primary Bi beam was split into 4 small pulses (Burst mode) providing a mass resolution of the order of $M/\Delta M$ ~6000 (measured on the Si peak).

The polished surface of specimen was slightly sputtered by a 45° 2 keV Cs^+ beam delivering a 100 nA current to remove the native oxide layer in order to perform 2D imaging of the metallic substrate in positive polarity using a 25 keV pulsed primary Bi^+ beam delivering 0.1 pA. The conditions of removal of the native oxide were optimized by repeated depth profiling experiments on the same sample but in different sample regions. Then, for the corroded specimen, 3D imaging was performed in negative polarity using the same Cs^+ sputtering beam and a 25 keV primary Bi^+ beam delivering 0.3 pA. Lateral shift correction on the all reconstructed 3D images were automatically done on the Cl^- images. using the Ion-Spec software. A schematic presentation of the principle of 3D ToF-SIMS chemical mapping based on 2D successive maps recorded after sputtered layers from the sample surface to the oxide/metal interface over the sputtering depth of 300 s is shown in Fig.1. The sputtering time between each 2D chemical mapping was 4 s. The final reconstructed 3D chemical mapping represents a stack of 2D maps performed at different depths. For both measurements (2D and 3D), the sputtered area was 1000 μm × 1000 μm and the analyzed area was 50 μm × 50 μm. Treatment of ToF-SIMS data was performed with Ion-Spec software (version 6.8). The 3D ToF-SIMS chemical image of one ion or several superimposed ion signals can be represented as a 3D view (cube), and a plane view (by stacking 2D images at different depths).

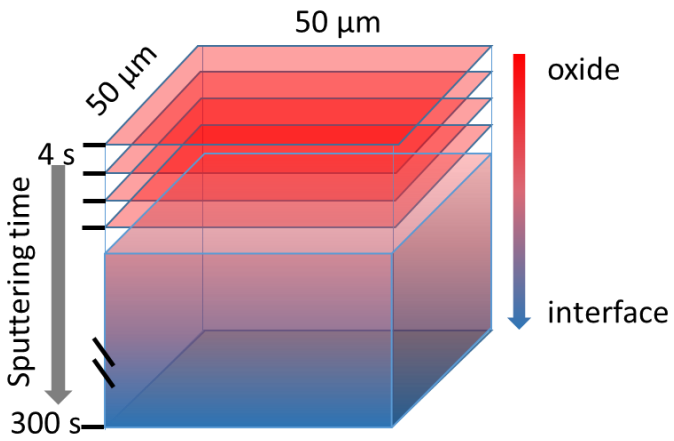

Figure 1: Schematic illustration of the principle of 3D ToF-SIMS imaging. Successive 2D chemical images (with size of 50 µm x 50 µm) were acquired at each 4 s of sputtering (in total 76 images) from the extreme surface to the alloy interface (corresponding to 300 s of in-depth sputtering). These 2D images are overlayed to generate a three-dimensional (3D) visualization of the sputtered volume. The images were performed in the defined area ROI comprising the IMPs and the matrix of AA 2024-T8 sample after corrosion test.

Microstructure characterization

SEM and EDX measurement were performed using the Zeiss Ultra55 SEM to easily define a region of interest comprising an Al-Fe-Cu-Mn IMPs and surrounding matrix and study the morphological modifications induced by immersion in 0.1M NaCl electrolyte.

3 Results and discussion

The SEM images with the same samples' area (ROI) including Al-Cu-Fe-Mn IMPs before and after corrosion are presented in Fig. 2(a, b) and (c,d). The EDX analysis performed in the in the bottom part of the IMPs (as indicated in (Fig. 2(b)by a green rectangle) shows that the chemical composition was 71.7 at% Al, 13.3 at% Cu, 7.5 at% Fe and 7.5 at% Mn. However, the chemical composition of IMPs is heterogeneous because of the visible contrast similar to those observed previously [46,47]. The EDX analysis of different particles (not presented here) showed the

enrichment in Cu and Fe for the brighter particles or brighter parts of particles. The quantity of Cu and Fe can be around 16.7±2.2 at% and 6.7±1.0 at%, respectively.

Next, the same sample region as presented in Fig. 2 (a) was analyzed by ToF-SIMS 2D chemical mapping using a positive mode, which is more sensitive to metallic species [38, 36]. Before analysis, the native oxide layer present on the surface of AA2050 was removed by a slight sputtering. As expected, ToF-SIMS 2D chemical mapping shows a high intensity of Cu^+, Fe^+, Mn^+ signals, and lower intensity of Al^+ in the area of IMP confirming the EDX results that the selected IMP is a typical Al-Cu-Fe-Mn phase. The advantage of ToF-SIMS over the EDX is a possibility to detect the low weight elements such as Li. Lower intensity of Li signal observed in ToF-SISM 2D mapping (Fig. 3, Li^+) in Al-Fe-Cu-Mn IMPs compared to the alloy matrix, indicates that Li is dissolved in the matrix. This can be confirmed by our previous TEM results [48], and other bibliographic data [49], showing that Li in AA2050-T8 is principally observed in the T1 phase (Al_2CuLi), which is homogeneously distributed in the matrix. However, other studies by Electron energy-loss spectroscopy (EELS) [50] and soft X-Ray emission spectroscopy [51] showed that Li can observed in the Al-Fe-Cu-Mn.

After immersion of AA2050-T8 sample in 0.1M NaCl electrolyte for 45 min initiation of corrosion over the Al-Cu-Fe-Mn IMPs and a trenching around the IMPs can be observed as shown in SE image in Fig. 2(d). The BE image (in Fig. 2 (c)) does not show clear modifications with reference to the pristine sample (Fig. (a) and (b)). The corrosion of aluminium alloys occurs by an enhanced dissolution of Al and/or lightweight elements from the Al alloy matrix close to the Al-Cu-Fe-Mn IMPs, which is induced by the galvanic coupling between the cathodic IMPs and more anodic alloy matrix [52,53] especially during the first stages of corrosion. However, it should be noted that the compositional heterogeneity within the IMP mentioned above, (Fig. 2a) can result also in initiation of localized corrosion attack inside the IMP as observed by SEM in Fig. 2b and as reported previously [46,54].

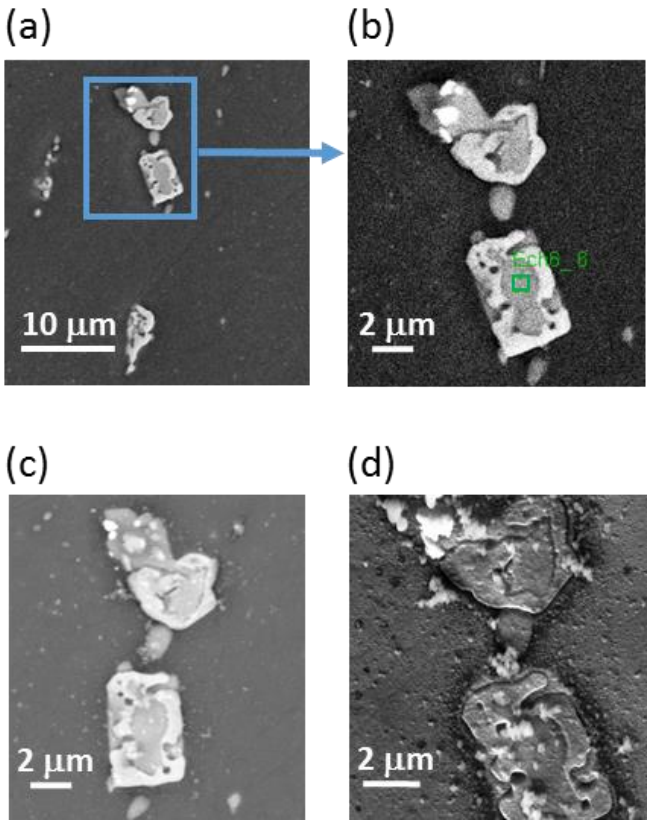

Figure 2: SEM images in a region containing Al-Fe-Cu-Mn IMP before immersion (a, b) and after immersion in 0.1M NaCl for 45 min (c, d); (a) SE image showing the whole ROI, (b) BE image with the rectangle showing the EDX analysis area, (c) BE and (d) SE images. The image (a) corresponds to the 2D and 3 D ToF-SIMS images presented hereafter, the images (b)-(c) are the magnified area of the blue rectangle zone shown in figure (a).

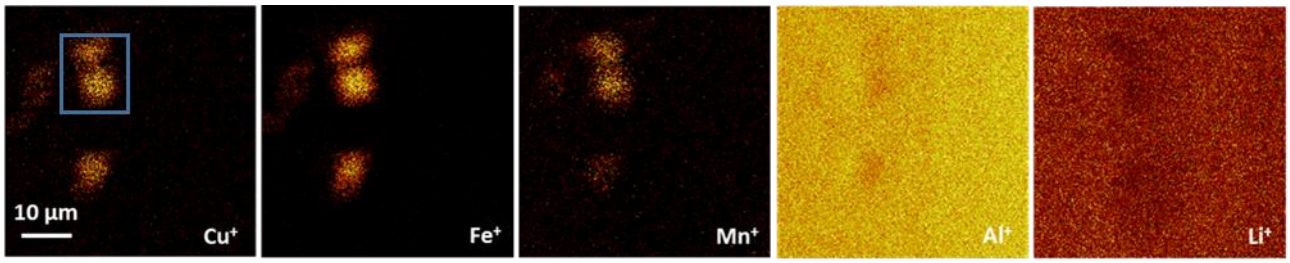

Figure 3: ToF-SIMS 2D chemical images (50 μm × 50 μm) of Cu^+, Fe^+, Mn^+, Al^+, Li^+ positive ions on the pristine AA2050-T8 sample in the ROI comprising selected Al-Fe-Cu-Mn IMPs before immersion test. A blue rectangle marked in the Cu^+ image corresponds exactly to the region of SEM micrograph presented in Fig. 2 (b-d).

ToF-SIM 3D chemical images in the same surface area of the sample after corrosion were obtained (Fig. 4), by acquiring the 2D successive chemical maps (50 μm × 50 μm × 300 s). Fig. 4(a) (b) and (c) show the 3D maps of AlO_2^- (m = 58.9728 u), AlO_2H^- (m=59.9812 u) and Al_2^- (m = 53.9634 u) signals. These signals are characteristic of Al oxide [36,38,40,41], Al hydroxide and Al metal, respectively. According to Fig. 4(a) and (b), the 3D image of AlO_2^- and AlO_2H^- show a homogeneous and high intensity of Al oxide/hydroxide signal over the whole analyzed volume. The lower intensity of AlO_2^- signal over IMPs region presented in the plane view of 3D image can correspond to the morphology effect of corroded surface and/or the oxide breakdown over this area. In Fig. 4(c) the increased intensity of Al_2^- in the bottom of the cube of matrix region (at the oxide/metal interface after 300 s of sputtering) can be observed but not over the IMPs region. The difference of Al_2^- intensity means that within the sputtering depths (300 s), the oxide/substrate interface in the area of IMP has not been reached but the oxide/substrate interface was reached in the matrix region. It should be noticed also that the lower Al^-_2 signal intensity over the IMPs after 300 s of sputtering can be also influenced by preferential dissolution of Al induced by the initiation of localized corrosion and/or a lower quantity of Al in the IMPs than in the alloy matrix. The differences in the intensity of Al_2^- in the area of IMPs and matrix will be discussed hereafter.

Cl^- (m = 34.9696 u) and OH^- (m = 17.0048 u) images are shown in Fig. 4 (d) and (e) to evidence the corrosion products and some residues of NaCl. Cl^- is present on the extreme surface (green signal in the top of cube) and then, deeper within the oxide layer, is found only locally over the IMPs region. The local Cl enrichment over the IMPs inside the oxide layer can be confirmed from the overlapping of the Cl^- (green in Fig. 4(d)) and Cu^- signals (orange in Fig. 4(f)), where the Cu^- signal corresponds to the Cu-rich IMPs. This higher intensity of Cl^- over the IMPs is clearly observed in the plane view map of Cl^-. Moreover, a slightly higher intensity of OH^- (Fig. 4(e)) is also observed in the bulk of the oxide in the IMPs region. Differently to the distribution of Cl^-, some OH^- signal is also observed in the matrix region. The presence of OH^- in the matrix over the whole depth of the oxide corroborates with the high intensity of AlO_2H^-. The chlorides and hydroxides over the corroded area confirms the localised corrosion as usually reported in the literature [38,55,56]. However, here for the first time, we demonstrate a local distribution of the Cl and OH in the bulk of the oxide layer, over the zones corresponding to the Cu-rich IMPs.

Cu^- (m = 62.9268 u), $CuOH^-$ (m = 79.9354 u) and Li^- (m = 7.0168 u) signals are also present to represent the distribution of the principle alloying elements. Cu^- and $CuOH^-$ ion signals (Fig. 4(f) and (g), respectively) show higher intensities over IMP region through the oxide layer, similar to

the Cl^- and OH^- signals. The enrichment in more noble elements such as Cu on the surface of corroded areas was reported previously [9,57-60]. The origin of this enrichment can be the preferential dissolution of Al induced by local submicron sized compositional heterogeneities within the IMP. Here, our results show that $CuOH^-$ signal in the matrix region is lower than in the intermetallic particle region (plane view image in Fig. 4(g)). The spatial distribution of OH^- is similar to $CuOH^-$, indicating that copper hydroxide is one of the corrosion products. Moreover, within the oxide layer (cube view images), the higher intensities of OH^- and $CuOH^-$ signals over the IMPs regions can be confirmed. In the case of Cu^- (cube view image in Fig. 4(f)), a more intense signal is observed not only over the IMPs region within the oxide but also at the oxide/metal interface. The Cu enrichment at this interface indicates the presence of metallic copper in the alloy substrate.

Fig. 4(h) shows a homogenous distribution of Li through the oxide layer in the 3D image of Li^- signal (m = 7.0168 u). However, the plane view clearly shows that almost no or a very low Li signal is observed over the IMPs, indicating a local Li dissolution. These results agree with our previous findings where no Li was observed in the area of corrosion [38]. However, the lower signal intensity over the IMP can also be a result of sputtering time not sufficient to reach the oxide /metal interface over this region or preferential dissolution of Al and other light elements like Li in the corrosion zone comprising the IMPs.

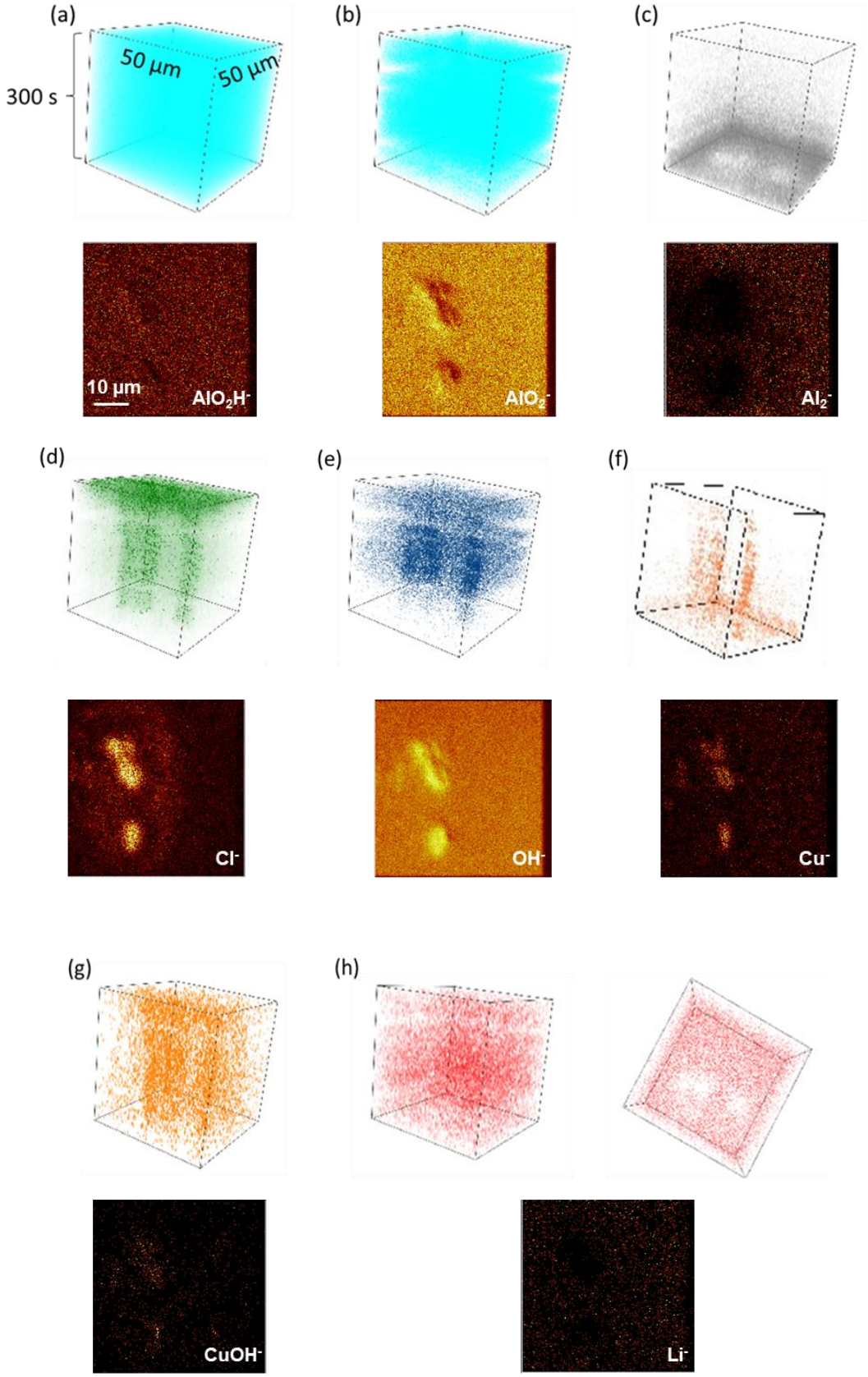
(a)
300 s
50 µm
50 µm
(b)
(c)
10 µm
AlO2H-
AlO2-
Al2-
(d)
(e)
(f)
Cl-
OH-
Cu-
(g)
(h)
CuOH-
Li-

Figure 4: ToF-SIMS 3D chemical images (50 µm × 50 µm × 300 s) and corresponding plane views (by stacking 2D slices at different depths) for a) AlO_2H^-, b) AlO_2^-, c) Al_2^-, d) Cl^-, e) OH^-, f) Cu^-, g) $CuOH^-$, h) Li^- (additional 3D top view image) obtained on the corroded AA2050-T8 sample (after immersion in 0.1 M NaCl) in the ROI comprising a selected Al-Fe-Cu-Mn IMP.

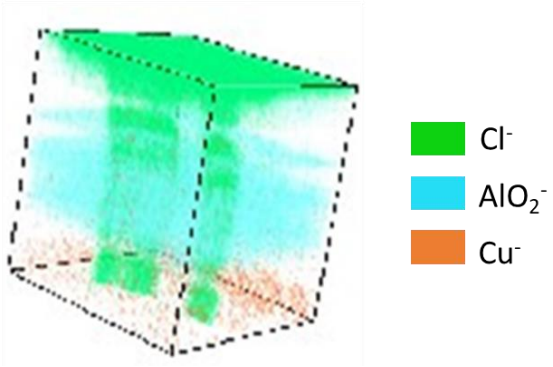

Figure 5: ToF-SIMS 3D map (50 μm × 50 μm × 300 s) showing the overlayed signals of AlO_2^- (blue), Cl^- (green) and Cu^- (orange) obtained on the corroded AA2050-T8 sample (after immersion in 0.1 M NaCl) in the ROI comprising a selected Al-Fe-Cu-Mn IMPs. The AlO_2^-, Cl^- and Cu^- signals are already presented individually in Fig. 4 (b), (d) and (f), respectively.

In order to compare the surface and bulk distribution of the most characteristic species, the AlO_2^-, Cl^- and Cu^- ions were overlayed and represented in one image (Fig. 5). The image treatment like the relative intensity changes of different signals was necessary to make all of them clearly visible. As discussed above (Fig.4 b), the AlO_2^- is observed in the whole analyzed volume. A significant difference in chemical composition can be observed between IMP and matrix region. The Cl^- signal shows a high intensity over the first seconds of sputtering corresponding to the top surface of the alloy and then the increased intensity is observed above Cu-rich intermetallic particle as observed previously for Al_2Cu IMPs in Al-Cu model alloy [40]. At the oxide/alloy substrate interface Cu enrichment is also observed over the matrix region.

To gain more insights into the differences between IMPs region and matrix after corrosion, the ion depth profiles were reconstructed from 3D images. As shown schematically in Fig. 6 (a), three regions can be distinguished on the AA2050 alloy after corrosion: the green matrix region

(A) ~78% of the total surface, the blue IMP region (B) ~2% and the rest, grey area (C), considered as the boundary between IMPs and matrix. The ion depth profiles corresponding to matrix (green, (A)) and IMPs (blue, (B)) were plotted separately to see in details the surface and bulk composition. The grey region (C) was excluded as a transitory region between the matrix and the IMPs. In order to be able to compare the intensity of different ions for IMP (Fig. 6 (b)) and matrix (Fig. 6 (c)) regions, the signal intensity was normalized.

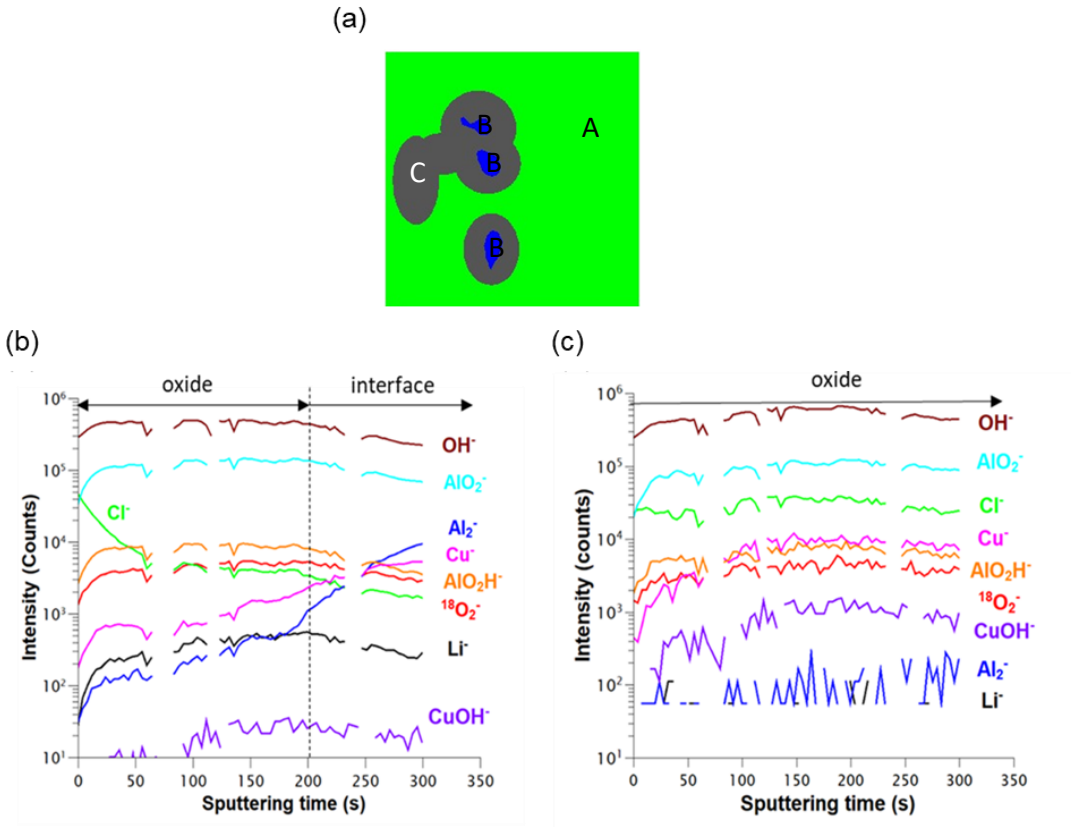

Figure 6: (a) Reconstructed ToF-SIMS 3D image of the same ROI presented in Fig. 3-5 showing three regions corresponding to matrix (green(A)), IMPs (blue(B)) and boundary between IMPs and matrix (grey(C)); (b) ToF-SIMS ion depth profiles of matrix region corresponding to the green area (A); (c) ToF-SIMS ion depth profiles of IMPs region corresponding to the blue area (B). The signal intensity was normalized by the analyzed area.

The signal intensity variations as a function of sputtering time reflect the modifications of the chemical composition and the in-depth structure of the analyzed oxide. OH^-, AlO_2H^- and AlO_2^- ion depth profiles for both matrix (Fig. 6 (c)) and IMPs (Fig. 6(d)) have similar intensity and shape,

which can indicate a similar chemical structure of the aluminium oxide/hydroxide layer over both regions. However, the low Al_2^- signal intensity in the area of IMPs (in Fig. 6 (c)) over the whole sputtering time (300 s), indicates a low quantity of metallic aluminium in the IMPs region induced by preferential dissolution of Al within the IMPs and that the oxide/metal substrate interface has not been reached after 300 s sputtering. In the case of the matrix region (Fig. 6 b), a step intensity increase of Al_2^- signal from 10^2 to 10^4 observed from 200 s of sputtering indicates that the interface with substrate region was almost attained. The longer sputtering time necessary to reach the oxide/metal interface for the IMPs can be related to the formation of corrosion layer with a different composition over the IMPs than the layer over the matrix region, like demonstrated in our previous work [38]. Using the same approach (3D ToF-SIMS chemical mapping), it was demonstrated that on the polished model Al-Cu alloy, the native oxide layer is thinner over the Cu-rich IMPs compared to Al matrix [40]. However, due to immersion in NaCl-based electrolyte, the large difference in corrosion potentials of more noble Cu-rich IMP and less noble Al-based matrix as well as local micrometric chemical heterogeneities within the IMPs (as shown in Fig. 2) leads to the localized cathodic and anodic reactions, respectively. As a consequence, the dissolution of the Al alloy in the vicinity of IMP and also to the preferential dissolution of Al inside the IMPs can occur leaving Cu remnant above IMPs. The Al dissolution can conduct to the particle dealloying [52]. The possible initially thinner oxide layer over the Cu-rich IMPs compared to Al matrix [40] can lead to a local high cathodic reactivity within the IMP and a high rate of oxygen reduction reaction, as shown by DFT calculations [61]. This implies the corrosion initiation in the areas enriched with noble elements like Cu (over IMP) and then the corrosion propagation with dissolution of Al matrix leading to the particles trenching as observed by time depended SKPFM studies on Al-Cu-Fe-Mn particles in AA7075-T6 [52]. In the further stages, both continuous cathodic and anodic reactions will enhance locally the formation of a new layer enriched with the corrosion products (chlorides and copper hydroxides as confirmed by Cl^-, Cu^- and $CuOH^-$ signals) over IMP and/or near IMP (Fig.6 (b) and (c)). The enrichment of the Cl^- through entire oxide layer above IMPs (Fig. 6(c)) while a rapid decrease of the Cl^- signal in the Al matrix from the top of surface to the interface is observed (Fig. 6(b)). The high intensity of Cu^- and $CuOH^-$ signals can be observed for IMPs (Fig. 6(c)). However, in the case of ion depth profiles obtained for the Al matrix region (Fig. 6(b)), a very low signal of $CuOH^-$ and the corresponding Cu^- signal keeps increasing from oxide to the interface. The low intensity of $CuOH^-$ indicates the lack of corrosion in the area of matrix, and the increased intensity of Cu^- at the oxide/substrate interface shows the presence of metallic Cu in the substrate.

A significant difference between the depth profile of Li in the IMPs and in the matrix is observed. Li is detected in the oxide layer on the matrix (Fig. 6 (b)) while no trace of Li was found in the IMP region (Fig. 6(c)). The presence of Li in the oxide over the matrix can be explained by a high stability of the oxide and no corrosion occurring in this area, which agrees with our previous results [38]. The lack of Li signal in the corrosion layer formed over the IMPs can indicate a dissolution of Li like discussed above (Fig. 4 (h)). However, it should be noted that lower Li signal intensity in the IMPs than in the matrix on the polished AA 2050 sample (Fig. 3) was already observed. The positive and negative ion intensities, performed on the pristine sample and corroded samples, respectively, cannot be directly compared.

It should be noted that these differences in the intensities of Cl^- and Cu^-, $CuOH^-$ and Li^- signals over the IMPs and matrix indicate some variations in the composition of layers formed in the two regions. The enrichment in these compounds confirms the localized corrosion occurring over the IMPs. In terms of principal compounds oxide (AlO_2^-, O_2^-) and hydroxide (OH^-) similar high intensities observed in both regions (Fig. 6) can indicate a similar composition of the layers. Small intensity increase of Cl^- and Cu^-, $CuOH^-$ and Li^- signals (where Cu-, and Li-based species are minor alloy compounds) cannot significantly influence the sputtering rate and induce large differences in sputtering times of layers over IMP and matrix. Since the sputtering time of the oxide above IMP is at least 1.5 times longer than that of the matrix, a higher thickness of the layer of IMPs can also be proposed. The formation of thicker layer over the IMPs induced by corrosion for the Al alloy was suggested previously. Davoodi *et al.* [16] used AFM/SECM to study the topography of corroded Al alloy and a greater height was observed on the IMPs, but this protrusion of the IMP was explained by their slower dissolution kinetics of the oxide layer over IMPs and the attack of IMPs. However, due to the limitation their analysis techniques, it was difficult to identify if the local protrusion was induced by the thicker oxide and/or the difference in the topography of metal substrate. With other techniques such as TEM or FIB-SEM, it is also difficult to detect the fragile oxide layer after corrosion especially if a particular and laborious sample handling and surface preparation are necessary. Cu enrichment and the enhanced oxide coverage was observed along the attacked Al-Cu-Fe-Mn particle/matrix interface region by SKPFM and AFM studies of AA7075-T6 corrosion [52]. Similarly, to the former studies, it can be concluded that here our results confirm the corrosion initiation attack over Al-Cu-Fe-Mn IMPs, which is associated with the higher quantity of noble elements (most particularly Cu) in the particles. It is followed by surface modifications with formation of corrosion layer with a different composition than over the matrix. Based on the results, the higher layer thickness over the IMPs can be also proposed, however to

firmly confirm this hypothesis further analyses are necessary. The dissolution of surrounding matrix can occur in further stages of corrosion.

The combined different modes of ToF-SIMS characterization (3D imaging and ion-depth profiling) allowed to have more insights into the mechanisms of corrosion initiation of AA2050-T8 alloy and to evidence structure and chemical composition of the layer over the IMPs and the alloy matrix.

4 Conclusions

In this paper, Tof-SIMS 3D chemical imaging was performed on AA2050 Al-Cu-Li alloy to observe the surface modifications induced by corrosion in 0.1M LiCl over the Al matrix and Al-Cu-Fe-Mn IMPs. A high sensitivity and high detection limit of ToF-SIMS allowed us to visualize a distribution of low atomic mass species like Li. No Li was observed in the oxide over the IMPs while trace of Li was detected in the oxide over the matrix. The ToF-SIMS 3D images and ion depth profiles, which can be retrieved from the images, can provide a better view on the lateral or in-depth distribution of different species. According to the ToF-SIMS ion depth profiles and 3D chemical mapping, a different oxide/hydroxide layer was formed over the IMPs where the localised corrosion attack was observed than the layer over the aluminium alloy matrix. The layer over the IMPs was thicker than over the Al matrix and enriched in Cl, OH and Cu.

Finally, it should be noted ToF-SIMS 3D imaging can be considered as a one of the most appropriate techniques to perform more systematic measurements on various IMPs and compared to alloy matrices in order to better understand the influence of substrate heterogeneity on the surface reactivity and the initiation and propagation of localised corrosion.

Competing Interest Statement

The authors declare no competing financial or non-financial interests.

Data Availability

The authors declare that the data supporting the findings of this study are available within the paper.

Author Contribution

Meicheng Li – experimental work, data analysis and interpretation, paper first version writing

Frédéric Wiame – paper revising, data interpretation

Antoine Seyeux – ToF-SIMS measurements, analysis and paper revision

Philippe Marcus – paper revision, data interpretation

Jolanta Światowska – corresponding author, conceptualization, data analysis and interpretation, paper writing and corrections

Bibliography

1 Z. Szklarska-Śmialowska, Pitting corrosion of aluminum, Corrosion Science, 41(9), 1743– 1767 (1999).
2 K. S. Rao and K. P. Rao, Pitting corrosion of heat-treatable aluminium alloys and welds: a review, Trans. Indian Inst. Met, 57(6), 593–610 (2004).
3 M. Elboujdaini and R. Revie, Metallurgical factors in stress corrosion cracking (scc) and hydrogen-induced cracking (hic), Journal of solid state electrochemistry, 13(7), 1091–1099 (2009).
4 W.-T. Tsai and M.-S. Chen, Stress corrosion cracking behavior of 2205 duplex stainless steel in concentrated nacl solution, Corrosion science, 42(3), 545–559 (2000).
5 G. Chen, K.-C. Wan, M. Gao, R. Wei and T. Flournoy, Transition from pitting to fatigue crack growth—modeling of corrosion fatigue crack nucleation in a 2024-T3 aluminum alloy, Materials Science and Engineering: A, 219(1-2), 126–132 (1996).
6 K. Sankaran, R. Perez and K. Jata, Effects of pitting corrosion on the fatigue behavior of aluminum alloy 7075-T6: modeling and experimental studies, Materials Science and Engineering: A, 297(1-2), 223–229 (2001).
7 Y. H. Liew, C. Örnek, J. Pan, D. Thierry, S. Wijesinghe and D. J. Blackwood, In-Situ Time-Lapse SKPFM Investigation of Sensitized AA5083 Aluminum Alloy to Understand Localized Corrosion, Journal of the Electrochemical Society, 167, 141502 (2020).
8 N. Birbilis, M. Cavanaugh and R. Buchheit, Electrochemical behavior and localized corrosion associated with Al7Cu2Fe particles in aluminum alloy 7075-T651, Corrosion Science, 48(12), 4202–4215 (2006).
9 T. J. Leclère and R. C. Newman, Self-regulation of the cathodic reaction kinetics during corrosion of AlCu alloys, Journal of The Electrochemical Society, 149(2), B52–B56 (2002).
10 W. Zhang, G.S. Frankel, Transitions between pitting and intergranular corrosion in AA2024, Electrochimica Acta 48 (2003) 1193-1210.
11 A. Boag, A. Hughes, A. Glenn, T. Muster and D. McCulloch, Corrosion of AA2024-T3 Part I: Localised corrosion of isolated IM particles, Corrosion Science, 53(1), 17–26 (2011)
12 U. Trdan and J. Grum, SEM/EDS characterization of laser shock peening effect on localized corrosion of Al alloy in a near natural chloride environment, Corrosion Science, 82, 328–338 (2014).
13 A. Chemin, D. Marques, L. Bisanha, A. de Jesus Motheo, W. W. Bose Filho and C. O. F. Ruchert, Influence of Al7Cu2Fe intermetallic particles on the localized corrosion of high strength aluminum alloys, Materials & Design, 53, 118–123 (2014).
14 D. A., P. J., L. C. and N. S., Integrated AFM and SECM for in situ studies of localized corrosion of Al alloys, Electrochimica Acta, 52, 7697–7705 (2007).
15 R. Grilli, M. A. Baker, J. E. Castle, B. Dunn and J. F. Watts, Localized corrosion of a 2219 aluminium alloy exposed to a 3.5% NaCl solution, Corrosion Science, 52, 2855–2866 (2010)
16 A. Davoodi, J. Pan, C. Leygraf and S. Norgren, The role of intermetallic particles in localized corrosion of an aluminum alloy studied by SKPFM and integrated AFM/SECM, Journal of The Electrochemical Society, 155(5), C211–C218 (2008).
17 C. Örnek, C. Leygraf and Jinshan Pan, Real-Time Corrosion Monitoring of Aluminum Alloy Using Scanning Kelvin Probe Force Microscopy, Journal of the Electrochemical Society, 167, 081502 (2020).
18 D. S. Lidke and K. A. Lidke, Advances in high-resolution imaging–techniques for threedimensional imaging of cellular structures, Journal of cell science, 125(11), 2571–2580 (2012).
19 [A. J. Bushby, K. M. P'ng, R. D. Young, C. Pinali, C. Knupp and A. J. Quantock, Imaging threedimensional tissue architectures by focused ion beam scanning electron microscopy, Nature Protocols, 6(6), 845 (2011).
20 C. Egan, S. Jacques, M. Wilson, M. Veale, P. Seller, A. Beale, R. Pattrick, P. Withers and R. Cernik, 3D chemical imaging in the laboratory by hyperspectral x-ray computed tomography, Scientific reports, 5, 15979 (2015).
21 R. D. Hanna and R. A. Ketcham, X-ray computed tomography of planetary materials: A primer and review of recent studies, Geochemistry, 77(4), 547–572 (2017).
22 T. Hashimoto, X. Zhang, X. Zhou, P. Skeldon, S. Haigh and G. Thompson, Investigation of dealloying of s phase (Al2CuMg) in AA2024-T3 aluminium alloy using high resolution 2D and 3D electron imaging, Corrosion Science, 103, 157–164 (2016).
23 B. Mingo, R. Arrabal, A. Pardo, E. Matykina and P. Skeldon, 3D study of intermetallics and their effect on the corrosion morphology of rheocast aluminium alloy, Materials Characterization, 112, 122–128 (2016).
24 B. Mingo, R. Arrabal, A. Pardo, E. Matykina and P. Skeldon, 3D study of intermetallics and their effect on the corrosion morphology of rheocast aluminium alloy, Materials Characterization, 112, 122–128 (2016).

25 M. Laleh, A. E. Hughes, S. Yang, J. Li, W. Xu, I. Gibson and M. Y. Tan, Two and threedimensional characterisation of localised corrosion affected by lack-of-fusion pores in 316L stainless steel produced by selective laser melting, Corrosion Science, 165, 108394 (2020).
26 B. Chen, M. Guizar-Sicairos, G. Xiong, L. Shemilt, A. Diaz, J. Nutter, N. Burdet, S. Huo, J. Mancuso, A. Monteith et al., Three-dimensional structure analysis and percolation properties of a barrier marine coating, Scientific reports, 3, 1177 (2013).
27 P. Bleuet, P. Gergaud, L. Lemelle, R. Tucoulou, P. Cloetens, J. Susini, G. Delette and A. Simionovici, 3D chemical imaging based on a third-generation synchrotron source, TrAC Trends in Analytical Chemistry, 29(6), 518–527 (2010).
28 R. Vallabhaneni, T. J. Stannard, C. S. Kaira and N. Chawla, 3D X-ray microtomography and mechanical characterization of corrosion-induced damage in 7075 aluminium (Al) alloys, Corrosion Science, 139, 97–113 (2018).
29 S. Jung, M. Foston, U. C. Kalluri, G. A. Tuskan and A. J. Ragauskas, 3D chemical image using ToF-SIMS revealing the biopolymer component spatial and lateral distributions in biomass, Angewandte Chemie International Edition, 51(48), 12005–12008 (2012).
30 J. S. Fletcher, Latest applications of 3D Tof-SIMS bio-imaging, Biointerphases, 10(1), 018902 (2015).
31 L. Zheng, A. Wucher and N. Winograd, Chemically alternating Langmuir-Blodgett thin films as a model for molecular depth profiling by mass spectrometry, Journal of the American Society for Mass Spectrometry, 19(1), 96–102 (2011).
32 S. Vaidyanathan, J. S. Fletcher, R. Goodacre, N. P. Lockyer, J. Micklefield and J. C. Vickerman, Subsurface biomolecular imaging of streptomyces coelicolor using secondary ion mass spectrometry, Analytical chemistry, 80(6), 1942–1951 (2008).
33 J. S. Fletcher, S. Rabbani, A. Henderson, N. P. Lockyer and J. C. Vickerman, Threedimensional mass spectral imaging of HeLa-M cells–sample preparation, data interpretation and visualisation, Rapid Communications in Mass Spectrometry, 25(7), 925–932 (2011).
34 M. A. Robinson, D. J. Graham and D. G. Castner, ToF-SIMS depth profiling of cells: zcorrection, 3D imaging, and sputter rate of individual NIH/3T3 fibroblasts, Analytical chemistry, 84(11), 4880–4885 (2012).
35 E. Niehuis, R. Moellers, F. Kollmer, H. Arlinghaus, L. Bernard, H. J. Hug, S. Vranjkovic, R. Dianoux and A. Scheidemann, In-situ Tof-SIMS and SFM measurements providing true 3D chemical characterization of inorganic and organic nanostructures, Microscopy and Microanalysis, 20(S3), 2086–2087 (2014).
36 D. Mercier, J. Swiatowska, S. Zanna, A. Seyeux and P. Marcus, Role of segregated iron at grain boundaries on Mg corrosion, Journal of The Electrochemical Society, 165(2), C42–C49 (2018).
37 M. Esmaily, P. Malmberg, M. Shahabi-Navid, J. Svensson and L. Johansson, A ToF-SIMS investigation of the corrosion behavior of Mg alloy AM50 in atmospheric environments, Applied Surface Science, 360, 98–106 (2016).
38 M. Li, A. Seyeux, F. Wiame, P. Marcus and J. Światowska, Insights on the Al-Cu-Fe-Mn intermetallic particles induced pitting corrosion of Al-Cu-Li alloy, Corrosion Science, 176, 109040 (2020).
39 A.-I. Stoica, J. Swiatowska, A. Romaine, F. Di Franco, J. Qi, D. Mercier, A. Seyeux, S. Zanna and P. Marcus, Influence of post-treatment time of trivalent chromium protection coating on aluminium alloy 2024-T3 on improved corrosion resistance, Surface and Coatings Technology, 369, 186–197 (2019).
40 P. Cornette, S. Zanna, A. Seyeux, D. Costa and P. Marcus, The native oxide film on a model aluminium-copper alloy studied by XPS and Tof-SIMS, Corrosion Science, 174, 108837 (2020).
41 A. Seyeux, G. Frankel, N. Missert, K. Unocic, L. Klein, A. Galtayries and P. Marcus, Tof-SIMS imaging study of the early stages of corrosion in Al-Cu thin films, Journal of the Electrochemical Society, 158(6), C165 (2011).
42 R. N. Sodhi, Time-of-flight secondary ion mass spectrometry (ToF-SIMS):—versatility in chemical and imaging surface analysis, Analyst, 129(6), 483–487 (2004).
43 D. W. Heard, J. Boselli, R. Rioja, E. A. Marquis, R. Gauvin and M. Brochu, Interfacial morphology development and solute trapping behavior during rapid solidification of an Al–Li–Cu alloy, Acta Materialia, 61(5), 1571–1580 (2013).
44 J.-T. Li, J. Swiatowska, A. Seyeux, L. Huang, V. Maurice, S.-G. Sun and P. Marcus, XPS and ToF-SIMS study of Sn–Co alloy thin films as anode for lithium ion battery, Journal of Power Sources, 195(24), 8251–8257 (2010).
45 D. Golodnitsky, M. Nathan, V. Yufit, E. Strauss, K. Freedman, L. Burstein, A. Gladkich and E. Peled, Progress in three-dimensional (3D) Li-ion microbatteries, Solid State Ionics, 177(2632), 2811–2819 (2006).
46 A. Davoodi, J. Pan, C. Leygraf, R. Parvizi and S. Norgren, An insight into the influence of morphological and compositional heterogeneity of an individual intermetallic particle on aluminium alloy corrosion initiation, Materials and Corrosion, 64(3), 195–198 (2013).
47 A. Boag, A. Hughes, N. Wilson, A. Torpy, C. MacRae, A. Glenn and T. Muster, How complex is the microstructure of AA2024-T3?, Corrosion Science, 51(8), 1565–1568 (2009).
48 M. Li, F. Wiame, A. Seyeux, P. Marcus and J. Swiatowska, Effect of thermal oxidation on surface chemistry and elemental segregation of Al-Cu-Li alloy, Applied Surface Science, 534, 147633 (2020).
49 F. Viejo, A. Coy, F. García-García, M. Merino, Z. Liu, P. Skeldon and G. Thompson, Enhanced performance of the AA2050-T8 aluminium alloy following excimer laser surface melting and anodising processes, Thin Solid Films, 518, 2722–2731 (2010).
50 Y. Ma, X. Zhou, W. Huang, G. Thompson, X. Zhang, C. Luo and Z. Sun, Localized corrosion in AA2099-T83 aluminum-lithium alloy: The role of intermetallic particles, Materials Chemistry and Physics, 161, 201–210 (2015).

51 C. M. MacRae, A. E. Hughes, J. S. Laird, A. Glenn, N. C. Wilson, A. Torpy, M. A. Gibson, X. Zhou, N. Birbilis and G. E. Thompson, An examination of the composition and microstructure of coarse intermetallic particles in AA2099-T8, including Li detection, Microscopy and Microanalysis, 24(4), 325–341 (2018).
52 Y. Zhu, K. Sun and G. Frankel, Intermetallic phases in aluminum alloys and their roles in localized corrosion, Journal of The Electrochemical Society, 165(11), C807–C820 (2018).
53 C.-M. Liao and R. P. Wei, Galvanic coupling of model alloys to aluminum—a foundation for understanding particle-induced pitting in aluminum alloys, Electrochimica Acta, 45(6), 881– 888 (1999).
54 S. Ghosh, Effect of stress on initiation and propagation of localized corrosion in alumninium alloys, Ph.D. thesis, University of Birmingham (2008).
55 T. Boettcher, M. Rother, S. Liedtke, M. Ullrich, M. Bollmann, A. Pinkernelle, D. Gruber, H.-J. Funke, M. Kaiser, K. Lee et al., On the intermetallic corrosion of Cu-Al wire bonds, in 2010 12th Electronics Packaging Technology Conference, pp. 585–590, IEEE (2010).
56 R. Grilli, M. A. Baker, J. E. Castle, B. Dunn and J. F. Watts, Localized corrosion of a 2219 aluminium alloy exposed to a 3.5% nacl solution, Corrosion Science, 52(9), 2855–2866 (2010).
57 M. Yasuda, F. Weinberg and D. Tromans, Pitting corrosion of Al and Al-Cu single crystals, Journal of the Electrochemical Society, 137(12), 3708–3715 (1990).
58 X. Zhou, G. Thompson, H. Habazaki, K. Shimizu, P. Skeldon and G. Wood, Copper enrichment in Al-Cu alloys due to electropolishing and anodic oxidation, Thin Solid Films, 293(1-2), 327–332 (1997).
59 Y. Zhu and G. Frankel, Effect of major intermetallic particles on localized corrosion of aa2060t8, Corrosion, 75(1), 29–41 (2019).
60 L. Lacroix, L. Ressier, C. Blanc and G. Mankowski, Combination of afm, skpfm, and sims to study the corrosion behavior of s-phase particles in aa2024-t351, Journal of the Electrochemical Society, 155(4), C131 (2008).
61 D. Costa, T. Ribeiro, F. Mercuri, G. Pacchioni and P. Marcus, Atomistic modeling of corrosion resistance: a first principles study of o2 reduction on the al (111) surface covered with a thin hydroxylated alumina film, Advanced Materials Interfaces, 1(3), 1300072 (2014).